

REPORT DOCUMENTATION PAGE			Form Approved OMB NO. 0704-0188		
<p>The public reporting burden for this collection of information is estimated to average 1 hour per response, including the time for reviewing instructions, searching existing data sources, gathering and maintaining the data needed, and completing and reviewing the collection of information. Send comments regarding this burden estimate or any other aspect of this collection of information, including suggestions for reducing this burden, to Washington Headquarters Services, Directorate for Information Operations and Reports, 1215 Jefferson Davis Highway, Suite 1204, Arlington VA, 22202-4302. Respondents should be aware that notwithstanding any other provision of law, no person shall be subject to any penalty for failing to comply with a collection of information if it does not display a currently valid OMB control number.</p> <p>PLEASE DO NOT RETURN YOUR FORM TO THE ABOVE ADDRESS.</p>					
1. REPORT DATE (DD-MM-YYYY) 19-01-2008		2. REPORT TYPE Final Report		3. DATES COVERED (From - To) 1-Jul-2001 - 31-Dec-2007	
4. TITLE AND SUBTITLE Scalable Quantum Information Processing and Applications: Final Report			5a. CONTRACT NUMBER		
			5b. GRANT NUMBER DAAD19-01-C-0077		
			5c. PROGRAM ELEMENT NUMBER 6D10T2		
6. AUTHORS Richard S. Ross, Mark F. Gyure, Edward T. Croke, Geoffrey D. Simms, Chris Anderson, Robert Kosut			5d. PROJECT NUMBER		
			5e. TASK NUMBER		
			5f. WORK UNIT NUMBER		
7. PERFORMING ORGANIZATION NAMES AND ADDRESSES HRL Laboratories, LLC MS RL69 3011 Malibu Canyon Rd. Malibu, CA 90265 -			8. PERFORMING ORGANIZATION REPORT NUMBER		
9. SPONSORING/MONITORING AGENCY NAME(S) AND ADDRESS(ES) U.S. Army Research Office P.O. Box 12211 Research Triangle Park, NC 27709-2211			10. SPONSOR/MONITOR'S ACRONYM(S) ARO		
			11. SPONSOR/MONITOR'S REPORT NUMBER(S) 42670-PH-QC.3		
12. DISTRIBUTION AVAILABILITY STATEMENT Approved for Public Release; Distribution Unlimited					
13. SUPPLEMENTARY NOTES The views, opinions and/or findings contained in this report are those of the author(s) and should not be construed as an official Department of the Army position, policy or decision, unless so designated by other documentation.					
14. ABSTRACT The main goal of this program was to design, fabricate and test a semiconductor device capable of demonstrating the fundamental physics required for the realization of a spin-coherent, single photon transmitter/receiver system. These requirements included careful tailoring of the g factor for conduction band electrons in the InGaAs/InP materials system, and the confinement, detection and manipulation of single electrons under lithographically defined gates. In this final report, we will describe our major accomplishments.					
15. SUBJECT TERMS Quantum repeater, quantum computing, quantum information processing					
16. SECURITY CLASSIFICATION OF:		17. LIMITATION OF ABSTRACT		15. NUMBER OF PAGES	19a. NAME OF RESPONSIBLE PERSON
a. REPORT U	b. ABSTRACT U	c. THIS PAGE U	SAR		Mark Gyure
					19b. TELEPHONE NUMBER 310-317-5342

Report Title

Scalable Quantum Information Processing and Applications: Final Report

ABSTRACT

The main goal of this program was to design, fabricate and test a semiconductor device capable of demonstrating the fundamental physics required for the realization of a spin-coherent, single photon transmitter/receiver system. These requirements included careful tailoring of the g factor for conduction band electrons in the InGaAs/InP materials system, and the confinement, detection and manipulation of single electrons under lithographically defined gates. In this final report, we will describe our major accomplishments.

List of papers submitted or published that acknowledge ARO support during this reporting period. List the papers, including journal references, in the following categories:

(a) Papers published in peer-reviewed journals (N/A for none)

R.E. Caflisch, M.F. Gyure, H.D. Robinson and E. Yablonovitch, "Modeling, Design and Optimization of a Solid State Qubit", SIAM Journal of Applied Mathematics, Volume 65, Number 4 pp. 1285-1304, 2005

E.T. Croke, R.N. Schwartz, B. Shi, A.A. Narayanan, A.A. Kiselev and M.F. Gyure, "Direct electrical measurement of the electron g factor in ultra-thin InGaAs/InP single quantum wells", Microelectronics Journal 36, 379 (2005).

C. R. Anderson and T. C. Cecil, "A Fourier-Wachspress Method for Solving Helmholtz Equation in Three Dimensional Layered Domains". J. Computational Physics, Volume 205, Issue 2, p. 706-718, 2005

Number of Papers published in peer-reviewed journals: 3.00

(b) Papers published in non-peer-reviewed journals or in conference proceedings (N/A for none)

R. L. Kosut, I. A. Walmsley, H. Rabitz, "Optimal Experiment Design for Quantum State and Process Tomography and Hamiltonian Parameter Estimation", quant-ph/0411093.

R. L. Kosut, I. A. Walmsley, Y. Eldar, H. Rabitz, "Quantum State Detector Design: Optimal Worst-Case a posteriori Performance", quant-ph/0403150

Robert L. Kosut, Matthew Grace, Constantin Brif, Herschel Rabitz, "On the distance between unitary propagators of quantum systems of differing dimensions", quant-ph/0606064.

Robert L. Kosut, Daniel A. Lidar, "Quantum Error Correction via Convex Optimization", quant-ph/0606078.

Number of Papers published in non peer-reviewed journals: 4.00

(c) Presentations

“Scalable Quantum Information Processing Devices”, Mark F. Gyure, 32nd Winter Colloquium on the Physics of Quantum Electronics, Snowbird, UT, January 8, 2002.

“A double quantum well single charge electrometer”, Hans D. Robinson, Prabhakar Bandaru, Hideo Kosaka, Eli Yablonovitch, Russel E. Caflisch, Chris Anderson, Mark F. Gyure and Edward T. Croke, presented at the American Physical Society March Meeting, Indianapolis, IN.

“Electron Confinement and Correlation in Anisotropic Quantum Dot Structures”, Mark Gyure, Matt Borselli, Russel Caflisch, Hans Robinson and Eli Yablonovitch, presented at the Materials Research Society Fall Meeting, Boston, MA, December 4, 2002.

“Electron Confinement and Correlation in Anisotropic Quantum Dot Structures”, Mark F. Gyure and Matt Borselli, presented at the 2003 American Physical Society March Meeting, Austin, TX.

“Design and Optimization of a Qubit”, R. Caflisch, Conference on Applied Inv. Prob., Lake Arrowhead, IPAM, May 20, 2003.

“Adaptive Control of Quantum Computing and Information Systems”, R. L. Kosut, INTERNATIONAL CONFERENCE PHYSICS AND CONTROL (PhysCon 2003), August, 20-22, 2003 Saint-Petersburg, RUSSIA.

“Maximum Likelihood Identification of Quantum Systems for Control Design”, R. L. Kosut, 13th IFAC Symposium on System Identification, Rotterdam, Netherlands, August 2003.

“Design and Optimization of a Quantum Dot Qubit System”, R. Caflisch, Workshop on Computational Approaches to the Electronic Structure of Quantum Dots, Chicago, IL, September 24, 2003.

“Simulation of an integrated quantum dot/single charge electrometer device for quantum computing”, Mark F. Gyure, Workshop on Computational Approaches to the Electronic Structure of Quantum Dots, Chicago, IL, September 22, 2003.

“Design and Optimization of a Quantum Dot Qubit System”, R. Caflisch, Workshop on Inverse Problems in Materials, IPAM, October 12, 2003.

“Control & Identification of Quantum Computation & Information Systems”, R. Kosut, UCSB, October 2003.

“Quantum State Tomography: Estimation and Experiment design”, R. Kosut, IPAM, November 2003.

“Design and Optimization of a Quantum Dot Qubit System”, R. Caflisch, USC Applied Math. Seminar, September 27, 2004.

“Design and Optimization of a Quantum Dot Qubit System”, R. Caflisch, Reunion Conference for Mathematics for Nanoscale Science and Engineering, Lake Arrowhead, IPAM, June 11, 2004.

“Progress Toward Realizing a Solid State Quantum Repeater in the InGaAs/InP Materials System”, Mark F. Gyure and Ed T. Croke, Gordon Research Conference on Quantum Information Science, Ventura, CA, February 28, 2005.

“Identification of Quantum Systems: Maximum Likelihood and Optimal Experiment Design for State Tomography”, R. L. Kosut, presented at 16th IFAC WORLD CONGRESS, Prague, July 4-8, 2005.

“Observation of Sequential Single Electron Charging in Vertical Enhancement Mode Quantum Dot Devices”, Edward Croke, Mark Gyure and Geoffrey Simms, presented at the 2006 American Physical Society March Meeting, Baltimore MD.

“Analysis of Random Telegraph Signals from Vertical “Enhancement Mode” Quantum Dot Devices”, Mark Gyure, Geoffrey Simms, Richard Ross and Edward Croke, presented at the 2006 American Physical Society March Meeting, Baltimore MD.

“Calculated tunneling rates for single electron charging events in Vertical Enhancement Mode quantum dot devices”, Richard S. Ross, Chris R. Anderson, Mark F. Gyure, presented at the 2006 American Physical Society March Meeting, Baltimore MD.

“Vertical Enhancement Mode Quantum Dot Devices for Spin-Based Qubits”, Mark F. Gyure and Edward T. Croke, presented at Spintech IV, Wailea, HI, June 21, 2007

Number of Presentations: 20.00

Non Peer-Reviewed Conference Proceeding publications (other than abstracts):

Number of Non Peer-Reviewed Conference Proceeding publications (other than abstracts): 0

Peer-Reviewed Conference Proceeding publications (other than abstracts):

Number of Peer-Reviewed Conference Proceeding publications (other than abstracts): 0

(d) Manuscripts

E.T. Croke, M.F. Gyure, B. Shi, A.A. Narayanan, F.P. Stratton, I.I. Milosavljevic and R.N. Schwartz, "Characterization of Top-Gated InGaAs Quantum Dots with a Vertically Integrated Readout Channel in the Few-Electron Regime", to be submitted to Applied Physics Letters.

I.A. Fedorov, K. W. Kim, R. E. Caflisch and E. Yablonovitch, "A scalable quantum gate design for quantum computation", UCLA CAM report, August 2003.

C.R. Anderson and C.J. Elion, "Accelerated solutions of nonlinear equations using stabilized Runge-Kutta methods", UCLA CAM report, April 2004.

Number of Manuscripts: 3.00

Number of Inventions:

Graduate Students

<u>NAME</u>	<u>PERCENT SUPPORTED</u>
Chris Elion	0.00
FTE Equivalent:	0.00
Total Number:	1

Names of Post Doctorates

<u>NAME</u>	<u>PERCENT SUPPORTED</u>
Tom Cecil	0.00
FTE Equivalent:	0.00
Total Number:	1

Names of Faculty Supported

<u>NAME</u>	<u>PERCENT SUPPORTED</u>	National Academy Member
Russel Caflisch	0.17	No
Chris Anderson	0.17	No
FTE Equivalent:	0.34	
Total Number:	2	

Names of Under Graduate students supported

<u>NAME</u>	<u>PERCENT SUPPORTED</u>
FTE Equivalent:	
Total Number:	

Student Metrics

This section only applies to graduating undergraduates supported by this agreement in this reporting period

The number of undergraduates funded by this agreement who graduated during this period:	0.00
The number of undergraduates funded by this agreement who graduated during this period with a degree in science, mathematics, engineering, or technology fields:.....	0.00
The number of undergraduates funded by your agreement who graduated during this period and will continue to pursue a graduate or Ph.D. degree in science, mathematics, engineering, or technology fields:.....	0.00
Number of graduating undergraduates who achieved a 3.5 GPA to 4.0 (4.0 max scale):.....	0.00
Number of graduating undergraduates funded by a DoD funded Center of Excellence grant for Education, Research and Engineering:.....	0.00
The number of undergraduates funded by your agreement who graduated during this period and intend to work for the Department of Defense	0.00
The number of undergraduates funded by your agreement who graduated during this period and will receive scholarships or fellowships for further studies in science, mathematics, engineering or technology fields:	0.00

Names of Personnel receiving masters degrees

<u>NAME</u>
Total Number:

Names of personnel receiving PHDs

<u>NAME</u>
Total Number:

Names of other research staff

<u>NAME</u>	<u>PERCENT SUPPORTED</u>	
Mark Gyure	1.00	No
Ed Croke	1.00	No
Robert Kosut	0.50	No
Bin Shi	0.10	No
Jeong Moon	0.10	No
FTE Equivalent:	2.70	
Total Number:	5	

Sub Contractors (DD882)

1 a. University of California - Los Angeles

1 b. Office of Contract & Grant Adm

11000 Kinross Ave. Suite 102

Los Angeles CA 900951406

Sub Contractor Numbers (c): S-101275-B

Patent Clause Number (d-1): 52.227-12

Patent Date (d-2):

Work Description (e): Develop numerical methods for the simulation of few-electron semiconductor quantum dots

Sub Contract Award Date (f-1): 7/1/2001 12:00:00AM

Sub Contract Est Completion Date(f-2): 12/31/2006 12:00:00AM

1 a. University of California - Los Angeles

1 b. Contract and Grant Administration

11000 Kinross Ave., Suite 102

Los Angeles CA 900951406

Sub Contractor Numbers (c): S-101275-B

Patent Clause Number (d-1): 52.227-12

Patent Date (d-2):

Work Description (e): Develop numerical methods for the simulation of few-electron semiconductor quantum dots

Sub Contract Award Date (f-1): 7/1/2001 12:00:00AM

Sub Contract Est Completion Date(f-2): 12/31/2006 12:00:00AM

1 a. SC Solutions

1 b. 1261 Oakmead Parkway

Sunnyvale CA 94085

Sub Contractor Numbers (c): S-101287-B

Patent Clause Number (d-1): 52.227-12

Patent Date (d-2):

Work Description (e): Develop quantum control methodologies for electron spin-based quantum information processing

Sub Contract Award Date (f-1): 7/1/2001 12:00:00AM

Sub Contract Est Completion Date(f-2): 12/31/2006 12:00:00AM

Inventions (DD882)

Scalable Quantum Information Processing and Applications: Final Report

Mark F. Gyure, Edward T. Croke, Richard S. Ross and Geoffrey D. Simms, HRL Laboratories, LLC
Chris Anderson, Department of Mathematics, UCLA
Robert Kosut, SC Solutions Inc.

(1) Foreword

The main goal of this program was to design, fabricate and test a semiconductor device capable of demonstrating the fundamental physics required for the realization of a spin-coherent, single photon transmitter/receiver system. These requirements include first, careful tailoring of the g factor for conduction band electrons in the InGaAs/InP materials system, and second, the confinement, detection and manipulation of single electrons under lithographically defined gates. In this final report, we will review our original program objectives and describe our major accomplishments. In Section (4), we will summarize our accomplishments in a timeline chart, which will clearly show how our actual rate of progress compared with our proposed plan. Section (5) will detail the major accomplishments called out in the timeline chart. Later, we will present a self-evaluation, identifying the lessons learned and what we would have done differently. Finally, we will conclude by discussing the outstanding challenges left for semiconductor-based quantum information science and technology and offer our assessment of the future of this field.

(2) Table of Contents

(1) Foreword	1
(2) Table of Contents	1
(3) List of Appendixes, Illustrations and Tables	2
(4) Statement of the problem studied	3
(5) Summary of the most important results	5
(5.1) Theoretical accomplishments	5
(5.1.1) InGaAs/InP 2D model of confinement	5
(5.1.2) Restricted 3D model of top-gated quantum dot device	6
(5.1.3) Full quantum mechanical simulation of realistic top-gated device structures including readout channels	9
(5.2) Experimental accomplishments	11
(5.2.1) First demonstration of g factor engineered InGaAs/InP QWs with large g factor shifts	12
(5.2.2) Fabrication of top-gated air bridge device structures with sub-50 nm feature sizes	14
(5.2.3) Demonstration of single-electron sensitivity in top-gated InGaAs/InP quantum dot devices	16
(5.2.4) First demonstration of few-electron quantum dot spectroscopy using random telegraph analysis	18
(5.3) Control accomplishments	20
(6) Bibliography	23

(3) List of Appendixes, Illustrations and Tables

Appendixes

None

Illustrations

Figure 1: Schematic diagram showing the UCLA concept for the quantum repeater

Figure 2: Timeline summarizing our original program goals and our accomplishments

Figure 3: Device geometry for NextNano3 simulation of our device structure

Figure 4: Simulation results showing the conduction band edge z- and y-dependence at the x midpoint

Figure 5: Wavefunction amplitudes in the y-z plane at the x midpoint

Figure 6: Quantum well occupation as a function of assumed Schottky barrier and effective doping activation

Figure 7: The potential with the quantum wire embedded as an isosurface

Figure 8: The potential with the quantum wire and quantum dot embedded as isosurfaces

Figure 9: Longitudinal resistance (R_{xx}) vs. magnetic field for sample B (40 nm spacer thickness)

Figure 10: Electron-spin resonance (ESR) enhanced resistance plotted as a function of field

Figure 11: Electron-spin resonance (ESR) enhanced resistance plotted for different source power levels

Figure 12: Schematic diagram showing layer structure and doping profile for the nominal double quantum well structure

Figure 13: Shubnikov de-Haas oscillations before and after illumination with a red LED

Figure 14: Model and SEM image of the HRL prototype single-qubit logic gate (SQLG)

Figure 15: Differential conductance (dI/dV_{SD}) as a function of gate voltage for a 50 nm dot

Figure 16: dI/dV_{SD} obtained from the same device as described in Fig. 15 at a significantly reduced sweep rate and increased point density

Figure 17: Differential conductance vs. time under fixed bias conditions

Figure 18: Current vs. gate voltage for a SQLG device fabricated using a structure with a 15 nm spacer

Figure 19: Current as a function of time at fixed gate voltage

Figure 20: Lifetime of the N electron state (high current) vs. the N+1 electron state (low current) as a function of gate voltage

Tables

None

(4) Statement of the problem studied

In our original proposal, we described a program to validate the basic physics of a solid-state quantum repeater based on a design conceived at UCLA by Prof. Eli Yablonovitch (Fig. 1). The idea was that it should be possible to build a solid-state device consisting of simply a single-photon detector, three single-qubit logic gates, and a single-photon emitter, capable of executing the teleportation algorithm on an incident photon, and faithfully transmitting its quantum state to another repeater connected using conventional optical fiber. We argued that the device would work by first converting the incident photon polarization state into an electron spin state, allowing it to interact with the adjacent electron spins trapped under the single-qubit logic gates, and finally emitting an entangled photon from the single-photon emitter.

For the program, we proposed to demonstrate the fundamental physics of such a device, (1) that the g factor for electrons in an InGaAs/InP quantum well (QW) can be tailored through an appropriate choice of Ga composition and layer thickness and (2) that individual electrons can be trapped under an electrostatic gate electrode and detected by monitoring the conductance of an integrated readout channel. The motivation for choosing these particular demonstrations is described below. First, the single-photon detector must be able to take an unknown quantum state, represented as a photon polarization and create an electron-hole pair, for which the unknown state would be transmitted to the spin state of the electron (and not the hole). Therefore, the g factor for electrons must be close to zero and the g factor for holes must be large enough for the hole to be created with definite spin [1]. In a paper by Kiselev et al. [2], a process known as g factor engineering is described for the case of InGaAs QWs in InP. Through an appropriate choice of Ga composition and InGaAs layer thickness, the g factor of an electron trapped in the InGaAs layer was predicted to sample both the negative g factor of InGaAs and the positive g factor of InP, resulting in an effective g factor of zero. We therefore set as our first objective, to demonstrate g factor engineering in InGaAs/InP.

The second objective, to design, fabricate, and test a single-qubit logic gate, arises from the requirement that the repeater concept requires three trapped electrons, in order to execute the teleportation algorithm. We therefore set out to develop the theoretical basis for designing a top-gated, electrostatic quantum dot in InGaAs/InP. In addition, HRL has considerable expertise in the growth and processing of InGaAs/InP heterostructures and so we proposed a complementary experimental effort to fabricate and test prototype devices and look for evidence of single-electron capture. The choice of materials system was motivated by the desire for the repeater design to be compatible with photon energies typically used in conventional optical networks.

Below, in the timeline shown in Fig. 2 and in bulletized form, we summarize the principle scientific goals of the program, as laid out in our original proposal and plot our accomplishments as they were achieved throughout the course of the program.

Goals:

Theoretical:

- Program Year 1 – 2D Model for electron confinement in InGaAs/InP
- Program Year 2 – Full 3D model for electron confinement and overlap

UCLA Quantum Repeater Concept

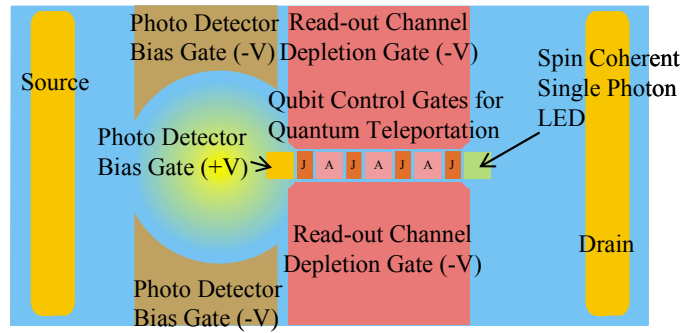


Figure 1: Schematic diagram showing the UCLA concept for the quantum repeater described in our original proposal. The design uses three single-qubit logic gates (labeled 'A'), a single-photon detector, and a single-photon emitter based in the InGaAs/InP materials system.

- Program Year 3 – Full 3D model for two-electron confinement
- Program Year 4 – Full 3D model with band structure
- Program Year 5 – Develop device simulations incorporating uncertainty

Experimental

- Program Year 1 – Measure the electron g factor in InGaAs/InP 2D electron gases
- Program Year 2 – Demonstrate single-electron sensitivity in quantum dot devices
- Program Year 3 – Demonstrate single-shot readout
- Program Year 4 – Demonstrate spin-dependent, single-photon detection
- Program Year 5 – Demonstrate spin exchange between two coupled dots

Accomplishments:

Theoretical

- InGaAs/InP 2D model of confinement
- Restricted 3D model of top-gated quantum dot device
- Full quantum mechanical simulation of realistic top-gated device structures including readout channels

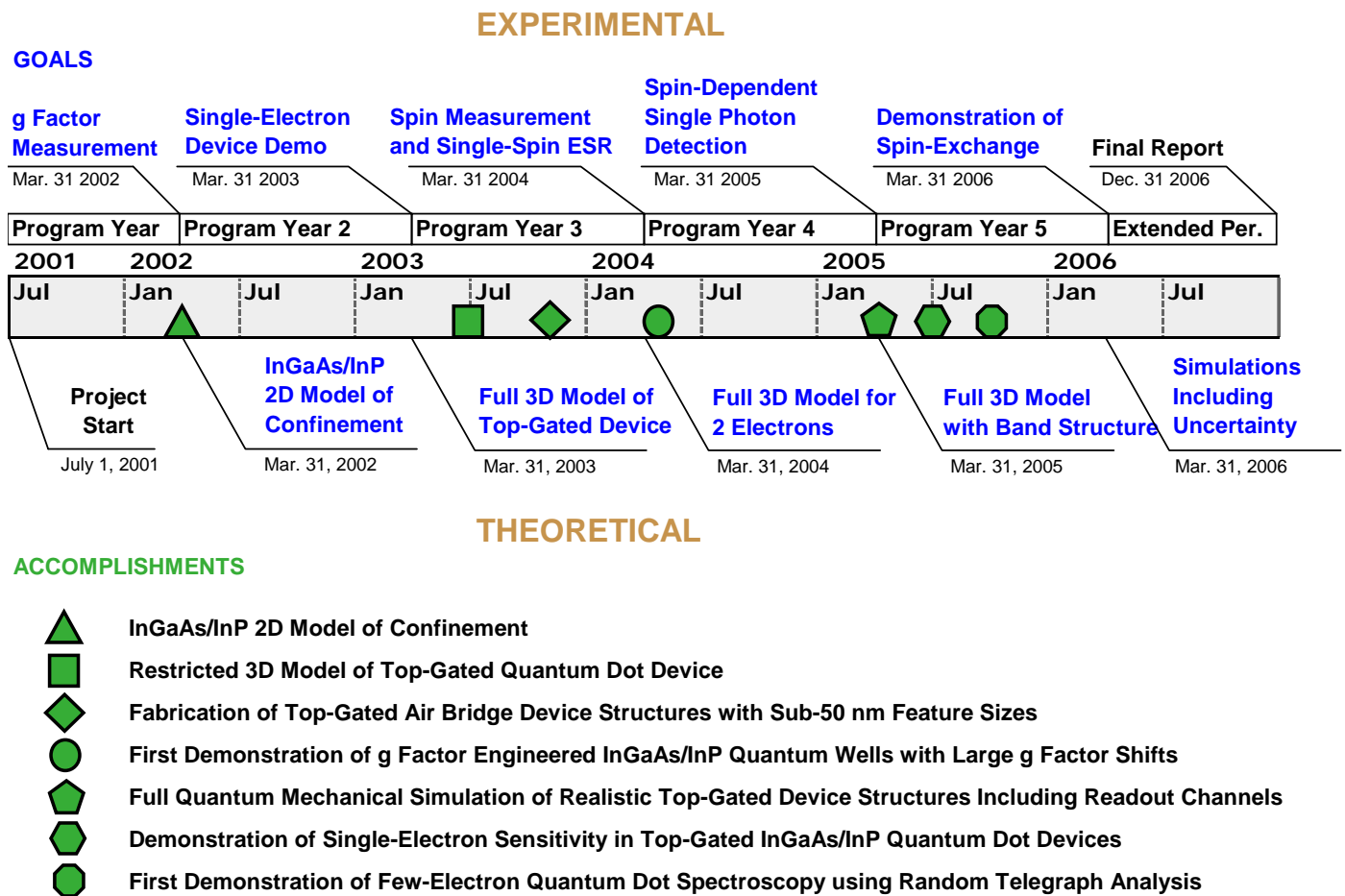


Figure 2: Timeline summarizing our original program goals (blue print) and our accomplishments (green markers) and their approximate date of accomplishment as they were achieved throughout the course of the program.

Experimental

- Fabrication of top-gated air-bridged device structures with sub-50 nm feature sizes
- First demonstration of g factor engineered InGaAs/InP QWs with large g factor shifts
- Demonstration of single-electron sensitivity in top-gated InGaAs/InP quantum dot devices
- First demonstration of few-electron quantum dot spectroscopy using random telegraph analysis

In Section (5), we describe in more detail the nature each of our major accomplishments.

(5) Summary of the most important results

(5.1) Theoretical accomplishments

The prototype single-qubit logic gate device we designed had to satisfy a large number of constraints that arise from engineering considerations as well as basic physics. The device must allow for the confinement of either one or zero electrons in an upper QW under reasonable gate voltage bias conditions while simultaneously allowing for a significantly depleted (and nearly one dimensional) 2D electron gas (2DEG) in the lower QW. The first condition is required in order to form an effective quantum dot for the electron whose spin state will serve as the qubit. The second condition arises from the fact that the current flowing through the lower QW (referred to as the channel) is sensitive to the presence of single charges in the vicinity of the channel only when severely depleted laterally by applying negative bias to a quantum point contact (QPC). Since this is our method for detecting the presence (or absence) of an electron in the quantum dot, satisfying this constraint was also critical.

(5.1.1) InGaAs/InP 2D model of confinement

The desired device has a “double pinchoff,” by which we mean that there is a single trapped electron in the quantum dot (in the upper QW) and a single transverse state in the quantum wire (in the lower QW). The electronic properties of this system are described by a Poisson equation for the electrostatic potential and a Schrödinger equation for the electron wave functions. Solution of the Schrödinger-Poisson equations for this system provides a method for assessing the double pinchoff property. The Schrödinger equation should have a single eigenvalue below the Fermi energy in the quantum dot and a single eigenvalue, corresponding to transverse eigenvector, below the Fermi energy in the QW. We used solutions of the Schrödinger-Poisson system as a design tool to find a design that attains the desired double pinchoff. This effort was critical to success of the project, since it would have been considerably more difficult to find a design by a purely experimental approach.

We developed two approaches to solution of the Schrödinger-Poisson system. The first is a direct numerical solution of the equations using a finite difference method. This has been carried out in one and two dimensions. The challenge of this problem is that the system is numerically stiff in the wells and that the nonlinear “self-consistent” terms (the contributions to the electrostatic potential from the electrons in the quantum dot and wire) make the eigenvalue problems nonlinear.

Our second approach was an approximation based on a combination of exact and approximate solutions of the Poisson and Schrödinger equations, for example the Schrödinger equation with square well and parabolic potentials, in one, two or three dimensions. This has not included self-consistent terms. From these approximations, a somewhat complicated but completely analytic formula (including a few iterative root finders) for the eigenvalues was obtained.

This latter method has been implemented in a Matlab program that allows for fast computation of proposed designs. As a first step, we searched a large design space and found 10 successful designs out of about 10 million trials. The resulting designs showed some surprising features; for example, the width of the two QWs were about equal, whereas we had expected the lower well (the channel) to be much wider. Based on these results, we narrowed the search and implemented a criterion for optimality of the design.

The direct numerical solution has been used to validate the analytic model and estimate the uncertainty in the results associated with the analytical modeling assumptions. In addition, the direct numerical simulation was used to understand the role of the choice of boundary conditions for the Schrödinger-Poisson equation. These boundary conditions are not clear from the physics, and we typically used conditions of prescribed potential on the top surface (corresponding to Schottky barrier offsets) and no flux on the bottom surface (corresponding to zero electric field at infinity). Alternate, seemingly reasonable boundary conditions exist, and the utility of these boundary conditions needs to be determined.

(5.1.2) Restricted 3D model of top-gated quantum dot device

The UCLA efforts on the direct numerical simulation of the coupled Schrödinger -Poisson equations have concentrated on the extension of the one and two-dimensional simulations to full three-dimensional simulations. The three dimensional simulation of the double well quantum device was completed and was validated against the Nextnano3 simulation tool that we obtained in late 2002 from the Theoretical Semiconductor Group at the Schottky Institute in Munich (Peter Vogl, director). The high computational efficiency of the UCLA simulation was obtained by exploiting the approximate separability of the model equations. Also, during the construction of this simulation, a new, robust, gradient free, iterative method for solving the consistent Schrödinger-Poisson equations was developed.

The starting point for the 3D device design was a structure identified using the Caflisch semi-analytic model. The challenge for this device is to achieve simultaneous depletion of the lower QW (as defined by the presence of only a few longitudinal quantum-wire-like states) and occupation of the upper well with a single state under low (<1V) forward (positive) bias conditions. The semi-analytic calculations produced optimal designs that were all very similar; variations from one optimal design to the next were, for the most part, almost within the experimental uncertainty in the parameters. A typical structure was input into NextNano3 and studied extensively over a range of gate voltages. Many numerical and modeling issues, such as code convergence, were addressed during the course of this analysis and extensive feedback

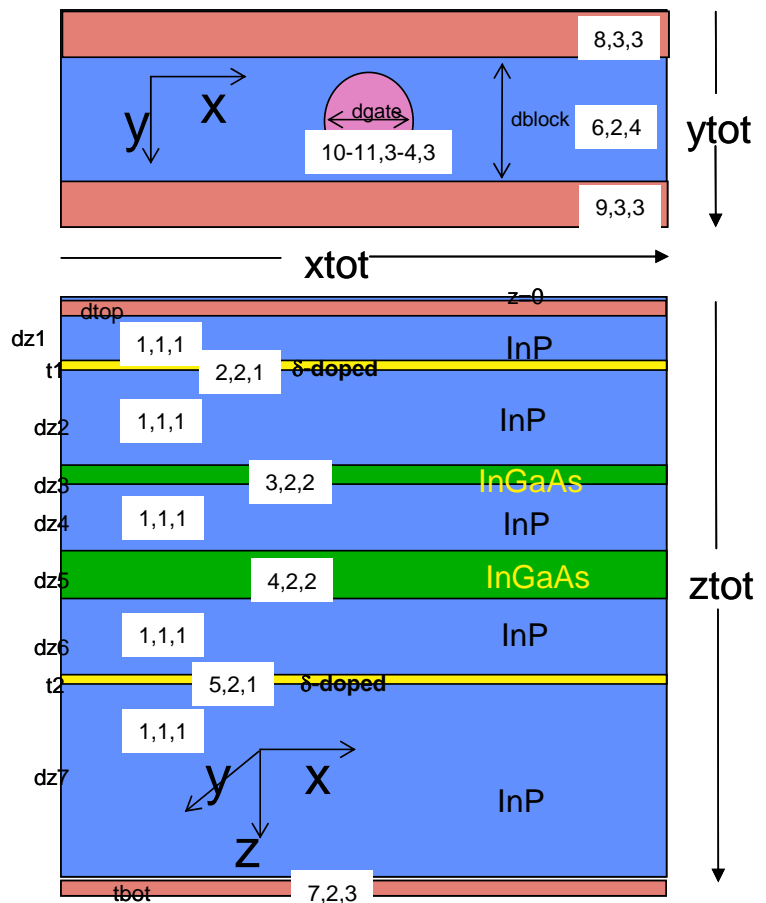


Figure 3: Device geometry for NextNano3 simulation of our device structure.

was given to the Vogl group related to bugs and desired improvements. The final results from NextNano3 indicated that, generally, states in the dot were harder to achieve, i.e. more forward bias on the dot gate was required for a given QPC voltage. This difference was attributed to the approximations inherent in the semi-analytic model.

Fig. 3 shows the device geometry that was used in the Nextnano3 simulation. Periodic boundary conditions are assumed in the x-direction, which is equivalent to making the assumption that the gates are infinitely long. For most of the devices fabricated, this is not a good assumption and the effect of realistic gate geometries was studied later. Realistic gate geometries can be generated with Nextnano3, but the large simulation size that is required makes the run times impractical (days to converge a single result). These simulations are possible with the UCLA code, however, because it is many times faster than Nextnano3. In the meantime, we felt that results using this geometry would still be perfectly useful as a first pass design tool. One issue regarding convergence of the results, we discovered, is the depth into the substrate below the last delta-doped layer (dz7 in Fig. 3). Using a background doping level for InP of 10^{-15} cm^{-3} (n-type) suggested by our device growers, the depth into the substrate needs to be quite substantial before the conduction band reaches its equilibrium value. Because Nextnano3 allows variable grid spacings within a region, however, this did not add any significant computational time to the simulations since the conduction band is changing smoothly in that region and a large grid spacing can be used.

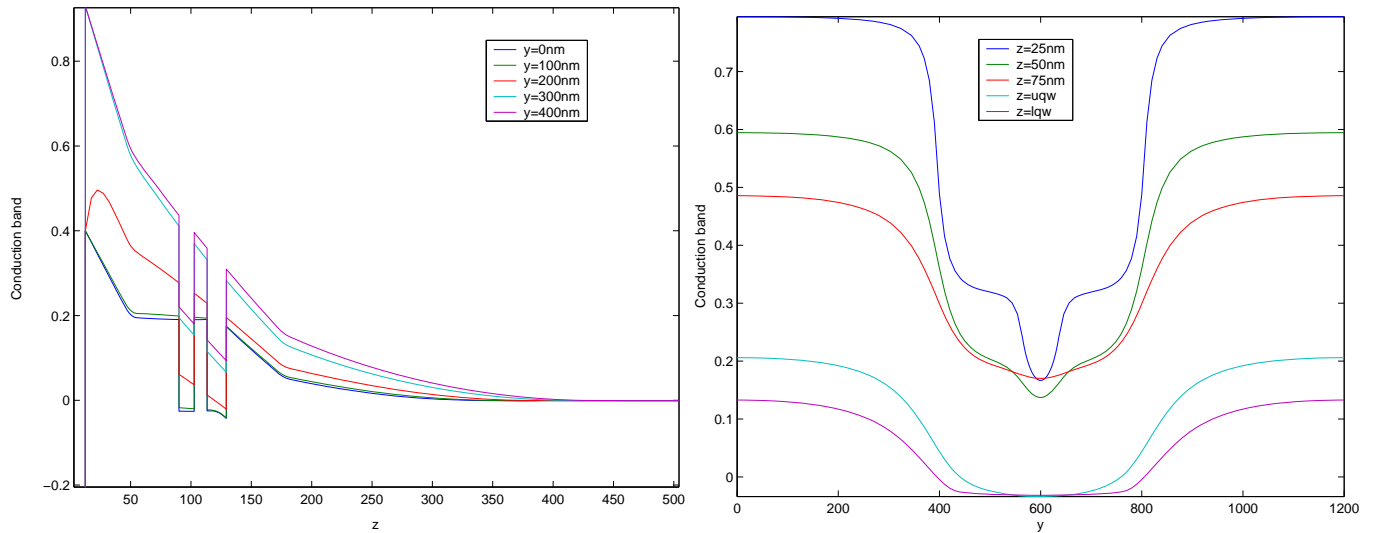


Figure 4: Conduction band edge z- (left) and y-dependence (right) at the x midpoint for the bias conditions given in the text.

Fig. 4 shows the conduction band edge produced by the simulation for a QPC voltage of -0.53V and a gate voltage of $+0.25\text{V}$. The left-most figure is the z-dependence of the conduction band at the x midpoint at various y values (see Fig. 3 for orientation of the axes). The right-most figure is the y-dependence of the conduction band, also at the x midpoint, at different values of z or depth into the structure. The most relevant feature in the z-dependence data is that both wells are only slightly below the Fermi level for y values that correspond to being nearly in between the QPC gates. The y-dependence data for different z values is more interesting. Here, the lower two curves are the conduction band in the center of the two QWs (upper well - green; lower well - purple). It is clearer here that the conduction band in both wells is below the Fermi level only in between the QPC gates and is at a depth where there are very few states. Also noticeable is that the effect of the dot gate is very small in both wells. On this voltage scale, it appears to be a concern that there is no real confinement due to the dot. On a finer scale, however, there is a clear potential well with a confinement depth of a few meV, more than deep enough to capture electrons at He^3 temperatures (250 mK).

Fig. 5 shows wavefunction amplitudes calculated by Nextnano for the bias conditions described above for several of the states just below the Fermi level. The amplitudes of the wavefunctions are color coded with blue representing zero and red representing the maximum value. They are shown in the y-z plane at the x midpoint with vertical being the y-direction and horizontal, the z-direction. The left side of each plot is the top of the device structure and moving to the right corresponds to moving down into the structure. Wavefunctions that have significant amplitudes toward the right side of each plot are localized in the lower QW, or channel. The one plot (105) that has most of the amplitude on the left side represents the one state of all those below the Fermi level that is localized in the upper well. This state represents two electrons (this calculation assumes degenerate spin states and no electron-electron interaction) in the quantum dot. Note that there are up to 12 occupied states in the y-direction the lower well for this case; the reason there are more than 100 occupied states total is due to the transverse states in the lower well that are really extended states in the x-direction

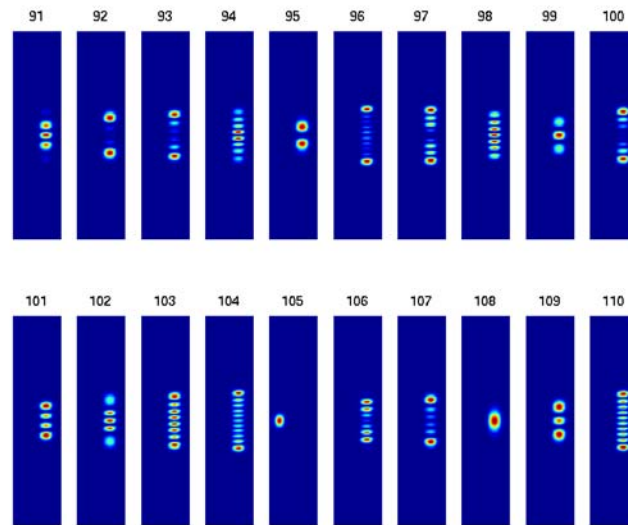


Figure 5: Wavefunction amplitudes in the y-z plane at the x midpoint for the bias conditions described in the text.

The semi-analytic calculation showed that the first dot state was present with fewer channel states. As mentioned previously, this is almost certainly due to the approximations inherent in that calculation. We have some concern that there may be too many states in the channel before the first dot state is present – the presence of many states in the lower well indicates that the channel is not close to depletion. It remains an open question whether, for this device, the channel needs to be almost completely depleted (i.e. only one or two states present) in order to be sensitive to single electrons. The channel is only 10nm from the electron, so we believe that it will be sensitive to single charges even when the channel is not near full depletion.

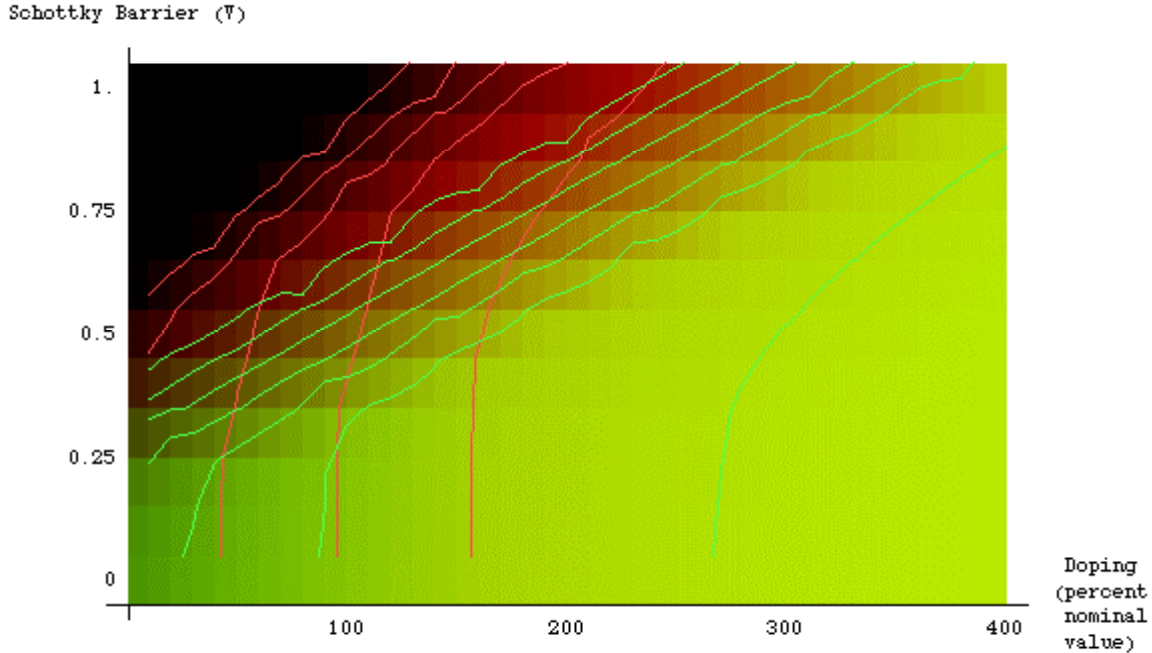


Figure 6: Quantum well occupation as a function of assumed Schottky barrier and effective doping activation

In order to parameterize our model with the experimental results, we calculated the QW occupations of several one-dimensional systems with Nextnano3, at a number of different doping values, assuming 100% activation of the dopants. We also allowed for a wide range of surface potentials, which could be interpreted as Schottky barriers plus a uniform applied gate voltage. The results are shown in Fig. 6. In this figure, the lower well occupation is indicated by the red color level, and the upper well by the green color level. When both wells are occupied, the figure shows a yellow color. The contour lines are shown separately for the lower well (red) and the upper well (green). The presence of lower well charge only indicates being up in the bright red region of the graph in Fig. 6, and is consistent with being somewhere between about 50 and no more than 200 on the horizontal axis. Our presumption that the Schottky value was around 0.75V would imply that the charge density in the lower well was very near the nominally designed value.

(5.1.3) Full quantum mechanical simulation of realistic top-gated device structures including readout channels

At the end of Program Year 4, we completed the implementation of a fully three-dimensional Poisson-Schrödinger solver for planar heterostructures with patterned metallic surface contacts. As distinct from the code developed at UCLA, this code is the baseline code into which we incorporated electron-electron interactions that allowed us to study in detail the spectroscopy of our gated quantum dots.

The self-consistent electrostatic potential and charge densities were computed following the method of Trellakis et.al. [3], in which a predictor-corrector scheme is employed. Specifically, the electrostatic potential is solved via the Poisson equation in which a trial (predictor) source charge density is used. The actual charge density is then computed via the Schrödinger equation (corrector) given this electrostatic potential. The predictor is derived from the fully quantum mechanical charge density by introducing a variation of the local Fermi energy

proportional to the local value of the current electrostatic potential. This predictor is thus a non-linear functional of the electrostatic potential and the resulting non-linear Poisson equation is solved via Newton's method. The electrostatic potential obtained is then used to compute a new charge density via the Schrödinger equation, the 'corrector' in the overall scheme. The eigenvalue problem associated with the discretized Schrödinger equation is the single most time consuming part of this scheme. We address this problem by first solving for the charge density quantum mechanically only in regions of our geometry for which discrete quantum states are of interest, namely the QW/dot regions. Second, we use an eigenvalue solver (ARPACK) which performs an iterative eigenvalue solve allowing us to only extract the lower lying eigenvalues of interest. We also worked with Chris Anderson at UCLA to incorporate his more efficient eigenvalue solver tailored specifically for this problem. We have implemented an exchange-correlation potential in the local density approximation (LDA) as a first step towards incorporating more exact many-body effects in this code. This is added as an additional local source term in the Schrödinger equation.

A unique aspect of our code is the discretization employed. The Schrödinger and Poisson equations are discretized using a high-order volume finite element scheme. Arbitrary order finite elements and solution accuracies are selectable via specially constructed numerical basis functions and quadrature rules. This will allow for more accurate solutions to be obtained with fewer unknowns, a serious concern when solving three-dimensional problems.

In previous reports, we highlighted the fact that the major computational bottleneck in the three dimensional simulation is the computation of the 3D quantum states and their associated energies (e.g. the eigenvectors and eigenvalues of the 3D Schrödinger operator). Most of the numerical work performed recently was dedicated to reducing this computational bottleneck. Several advances were made, the most notable were

- The construction of a robust iterative eigenvalue/eigenvector method; a method that is capable of handling problems in which the eigenvalues are very closely spaced or have multiplicity greater than one.
- The development and implementation of an adaptive basis technique to accelerate the computation of states associated with separable approximations to the Schrödinger operator.
- The development and implementation of an adaptive basis technique to accelerate the computation of states of the non-separable Schrödinger operator.

The development of the iterative method was necessitated by the fact that the states that must be computed in the simulation can have energies with multiplicity greater than one and are very close to each other in magnitude. The multiplicity arises because of the symmetry of the geometry and the close spacing arises because we are approximating a continuous spectrum when computing the states contributing to the quantum wire in the lower well. Both of these features cause problems when standard iterative methods are used and so we developed a new method by combining two existing procedures; subspace iteration with polynomial filtering. The method has the advantage of simplicity --- it is much less complicated than Lanczos's method and it does not require any form of "pre-conditioning" as Davidson's method or Inverse Subspace Iteration requires. Moreover, the method is implemented as a C++ template requiring only the specification of an operator class and a vector class. This form of C++ packaging has enabled us to use quickly incorporate the procedure into all of the existing simulations. The report describing the procedure is in the process of being written up.

The development of a robust iterative eigenvalue/eigenvector solver goes a long way towards removing the computational bottleneck, but computing large numbers of states associated with systems that have hundreds of thousands of unknowns is still very computationally demanding. One way to reduce the operation count is to

use a basis that can approximate the desired states, but has a dimension much smaller than the space associated with the standard basis. For example, if we knew the M states with energies less than the Fermi energy, and used those states as a basis, we could reduce the problem to one of dimension M . If M is on the order of hundreds, or thousands, the eigenvalue/eigenvector problem can be solved very quickly. Unfortunately, we don't know the states with the lowest energies --- that is what we are trying to find --- but we do know the potential. As a first approximation, the potential can be used to determine the support of the wave functions with lowest energies, and so the basis we use for the eigensystem computation is one whose support is determined by the potential. In the devices being investigated there is strong confinement in the vertical direction and in one transverse direction, so the basis set used has a much smaller dimension than the complete system and the computation time for the eigenvector/eigenvalue system is considerably reduced.

The above advances in the state computation have resulted in a computationally efficient simulation that provides design quality information for the quantum bit devices under investigation. Sample results that demonstrate the operational behavior of the device are depicted in Figs. 7 and 8. In Fig.7, an isosurface of the electron density is embedded in a visualization of the potential of the sample device. In this figure, the side gates are biased so that there is a quantum wire in the lower well and no states (e.g. dot) in the upper well. In Fig. 8, we show the electron density embedded in the device with the center gate biased to induce a dot in the upper well. (The isosurface of the dot in the upper well is of the same value as the lower well, but it is colored red to highlight its appearance.).

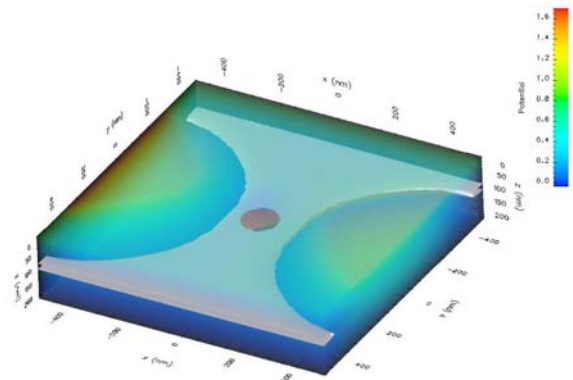
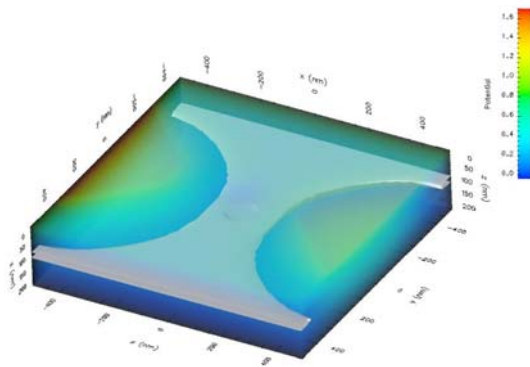


Figure 7: The potential with the quantum wire embedded as an isosurface.

Figure 8: The potential with the quantum wire and quantum dot embedded as isosurfaces.

(5.2) Experimental accomplishments

Throughout the course of this program, we have focused on two principal experimental objectives. The first, to measure the g factor of electrons confined to InGaAs QWs in InP, depended critically on our ability to model and fabricate devices (gated Hall bars) exhibiting a high carrier mobility and a controllable electron concentration (through the application of a gate voltage or by adjusting the dopant concentration). Our approach was to induce a resonance between the spin-split Landau levels of a 2DEG in a magnetic field through the use of a fixed frequency microwave source. At resonance, the magnetoresistance of the Hall bars we made showed an enhancement of the ρ_{xx} component of the resistivity tensor (as expected) due to spin-flips induced by the microwave field. The g factor was then calculated from the field, B , and the microwave frequency, ν , through the simple formula, $g=h\nu/\mu B$.

Our second objective was to demonstrate the detection of individual electrons trapped electrostatically in a lithographically defined quantum dot. Our approach was to use a double-QW structure in which two $\text{In}_{0.53}\text{Ga}_{0.47}\text{As}$ QWs surrounded by InP formed the confining layers for both the electron qubit (in the upper well) and the detecting layer (lower well). Doping was used above and below the double-QW structure to create a situation in which carriers were localized primarily in the lower well. A narrow channel was formed by applying a negative bias to a pair of depletion gates, the QPC, coming in from the side of a mesa etched through the double-QW structure. Positive bias was applied to form the quantum dot via an air-bridged gate which contacted the semiconductor through a small post typically less than 200 nm in diameter. In the following sections, we will discuss our experimental results with respect to these two objectives.

(5.2.1) First demonstration of g factor engineered InGaAs/InP QWs with large g factor shifts

The electronic g factor associated with electrons trapped in an InGaAs QW depends on the thickness of the QW and the composition of the surrounding materials (in this case, InP). In the experiments we have been conducting, 30-40 GHz microwaves were launched onto a microstrip resonator fabricated on a Rogers 5880 laminate substrate. The end of the microstrip was terminated with a short, and so, we positioned the sample at a location approximately one-half wavelength from the end of the microstrip to maximize the magnetic component of the microwave field (\mathbf{B}_1) seen by the sample. This configuration ensured the proper orientation of the microwave magnetic field and the external static field \mathbf{B}_0 (namely $\mathbf{B}_1 \perp \mathbf{B}_0$) to observe electron spin resonance (ESR). In the experiment, we measured the component of the g tensor parallel to the static field by monitoring the longitudinal resistance of the sample at resonance. In order to observe the resonance, the sample must have a high mobility to allow spin-splitting to be resolvable at the resonant field.

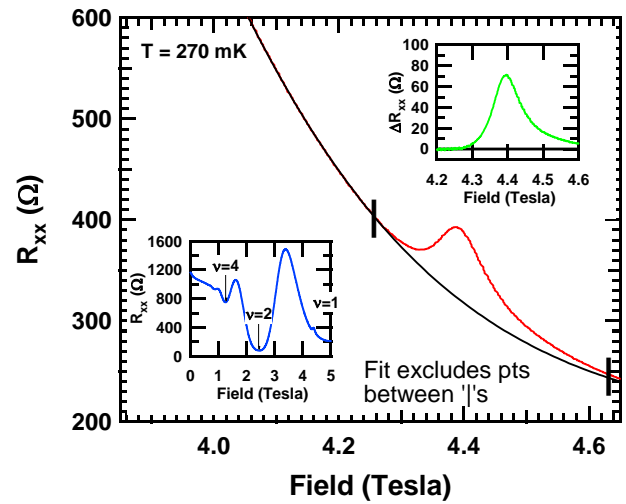


Figure 9: Longitudinal resistance (R_{xx}) vs. magnetic field for sample B (40 nm spacer thickness). 38 GHz microwaves were applied using +10 dBm source power, producing a resonant enhancement of the resistance near 4.4 T. The resonant field was obtained from the raw data after subtracting the non-resonant background (inset).

For this experiment, two single-QW samples were grown by MBE at HRL and prepared in the Van der Pauw geometry, approximately 0.25 in. square, in which slots were cut using a shadow mask and a sand blaster. The QW in each of the samples was 2.6 nm in thickness and composed of $\text{In}_{0.44}\text{Ga}_{0.56}\text{As}$. The spacer thickness was 30 nm for sample A and 40 nm for sample B. The resistance was measured using a PAR 124A lock-in amplifier, with the reference applied across the sample. For sample A, the carrier concentration was too high to observe spin-splitting at an accessible field. Somewhat serendipitously, the carrier concentration of sample B was just right, and the resonance was observable in the $\nu=1$ spin-split valley for microwave frequencies between 31 and 40 GHz, within the capabilities of our detection system.

For Fig. 9, we measured the longitudinal resistance (R_{xx}) of sample B as a function of magnetic field while 38 GHz microwaves were introduced to the microstrip resonator under the sample. Near 4.4 T, a resonant enhancement of R_{xx} was observed. The ESR signal (inset to Fig. 9) was obtained from the raw data after subtracting the non-resonant background.

In Fig. 10, the ESR signal from sample B is plotted for several different microwave frequencies. The source power was varied to maintain a sample temperature of 300 mK during each sweep. ESR data obtained from a phosphorus-doped Si reference sample was used to calibrate the magnetic field. During the calibration procedure, we measured a dependence of the resonant field on sweep rate, due apparently to an induced field generated by eddy currents in the dewar. The sweep rate used to obtain the data plotted in Fig. 2 (+0.32 T/min) was found to generate an induced field of 178 G. The resonant field was calculated by subtracting 178 G from the peak position at each frequency. The corrected values of the resonance fields (B_{res}) were then used to calculate the g factor at each frequency according to the expression $g = h\nu / \mu_B B_{res}$. The data are in agreement with the expression $g_{\parallel}(B, N) = g_{\parallel 0} - c(N + 1/2)B$, where N is the Landau level index. Our measurements indicate a value of -0.65 for $g_{\parallel 0}$ and 0.014 1/T for c .

The Overhauser effect is one possible source of error in our measurements of the g factor. It is particularly problematic in III-V semiconductors since all of the elements of columns III and V of the periodic table have non-zero nuclear spin. The effect arises from an interaction between the nuclear spins in the lattice and electron spins in the 2DEG, causing a temporary polarization of the nuclear lattice at resonance. The effect produces an additional magnetic field, B_N , resulting in a shift of B_{res} . The degree to which the nuclei are polarized determines B_N and the amount of shift observable in B_{res} . In Fig. 11, we have plotted the ESR signal at 38 GHz as a function of microwave power. A small shift (~ 200 G) was observable as the power was increased from 1 to 70 mW at the source. The direction of the shift is consistent with previous measurements of the Overhauser shift in the AlGaAs/GaAs materials system [4] although its magnitude is much smaller.

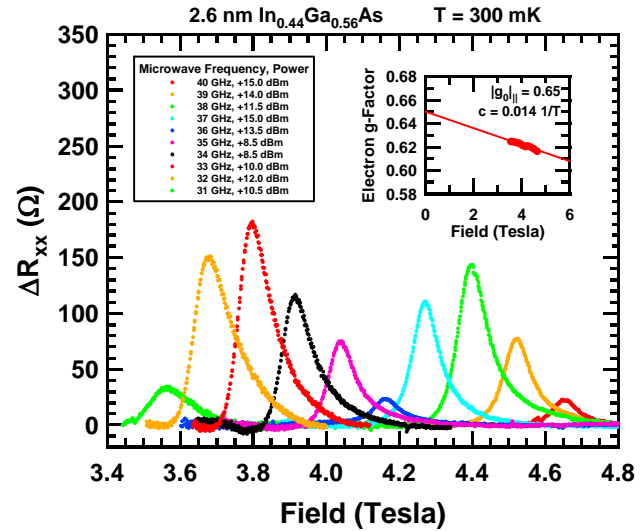


Figure 10: Electron-spin resonance (ESR) enhanced resistance plotted as a function of field after subtracting the non-resonant background for several applied microwave frequencies. The peaks were fit to a Gaussian function in order to extract the resonant field. An additional correction was applied to account for the field induced during the sweep through resonance. Calculated g -values are shown in the inset figure.

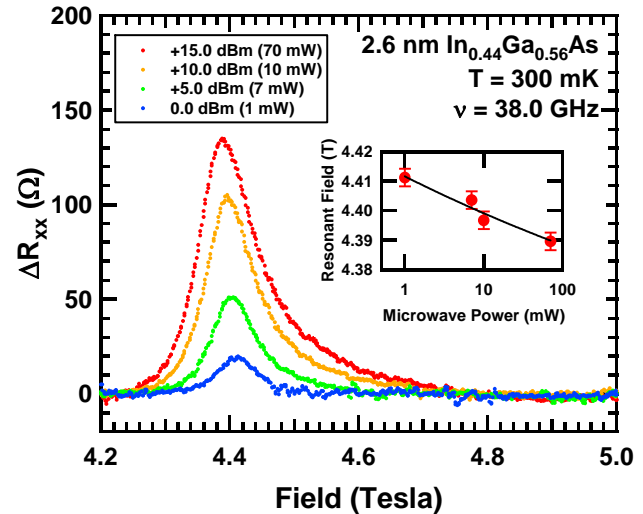


Figure 11: Electron-spin resonance (ESR) enhanced resistance plotted for different source power levels at 38 GHz. A small, 200 G shift is observable, consistent in direction with what might be expected due to the Overhauser effect.

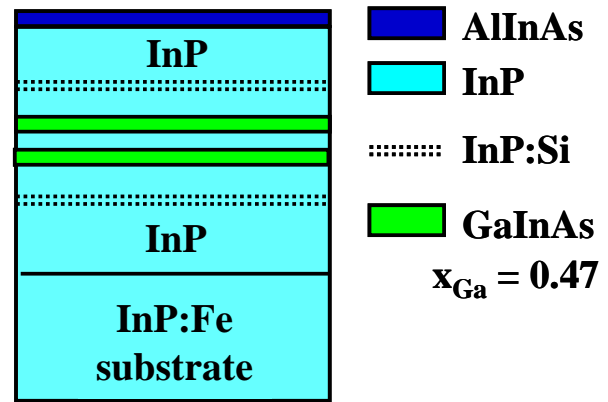
(5.2.2) Fabrication of top-gated air bridge device structures with sub-50 nm feature sizes

Our second objective was to demonstrate the detection of individual electrons trapped electrostatically under a lithographically defined gate. Our approach was to use the double QW structure shown schematically in Fig. 12. Two InGaAs QWs surrounded by InP form the confining layers for both the electron qubit (in the upper well) and the detecting layer (lower well). Delta doping was used above and below the double QW structure to create carriers localized in the lower well, resulting in a 2DEG. Input from our modeling team produced the nominal layer sequence shown in the table. In the experiment, an applied bias was used to pinch off the detecting layer laterally, nearly to the point at which it behaves like a QPC. The approach was anticipated to make the 2DEG highly sensitive to the presence of individual charges nearby. The electron was induced to tunnel from the detecting 2DEG and into the upper QW upon the application of a positive bias to an air-bridged gate, deposited directly on the AlInAs cap layer.

During this course of this program, we made significant progress addressing some nagging processing problems facing us in the past. First, we determined the annealing conditions necessary for creating low temperature ohmic contacts to the 2DEG. Second, we identified cleaning procedures prior to metal deposition that enhances adhesion, making possible contact to the devices via wire bonding. Finally, we perfected the photoresist layer deposition sequence and dosing parameters for electron beam lithography of sub-100 nm air-bridged structures that form the gate for our single-qubit logic devices.

Several samples were grown by molecular beam epitaxy according to the layer sequence shown in Fig. 12. A typical set of three wafers were labeled Q1, Q2, and Q3. The difference was in the doping as Q1 received the nominal amount, Q2 received 2x the nominal amount, and Q3 received 4x the nominal amount. One sample (doped like Q2) was selected for dicing and subsequent analysis. Hall mobility and magnetoresistance vs. magnetic field data confirmed this sample to be of excellent quality (mobility was $> 95,000 \text{ cm}^2/\text{V}\cdot\text{s}$), exhibiting numerous Shubnikov de-Haas oscillations with a carrier concentration of about $4 \times 10^{11} \text{ cm}^{-2}$ (about what we expected). The data are plotted in Fig. 13a, prior to illumination with a red LED. Sharp, spin-resolved Landau level oscillations were observed at fields as low as 2.5 Tesla.

Critical to the performance of our single-qubit logic gate (SQLG) is the requirement that only the lower well be filled below the free surface. In order to verify that this situation was indeed the case for the sample Q2, we illuminated a similar sample at low temperature and repeated the magnetic field sweep. The resulting data are shown in Fig. 13b. Clearly, the oscillations are considerably more complicated. However, we found that by



LAYER	MATERIAL	DOPING
200 Å	AlInAs	
155 Å	i-InP	
100 Å	n-InP	Si: 3.6×10^{17}
321 Å	i-InP	
126 Å	i-In _{0.53} Ga _{0.47} As	
106 Å	i-InP	
160 Å	i-In _{0.53} Ga _{0.47} As	
457 Å	i-InP	
100 Å	n-InP	Si: 1.3×10^{17}
5000 Å	i-InP	
InP substrate		

Figure 12: Schematic diagram showing layer structure and doping profile for the nominal double quantum well structure (Q1). Q2 and Q3 samples were grown essentially to the same parameters with 2x and 4x doping levels, respectively.

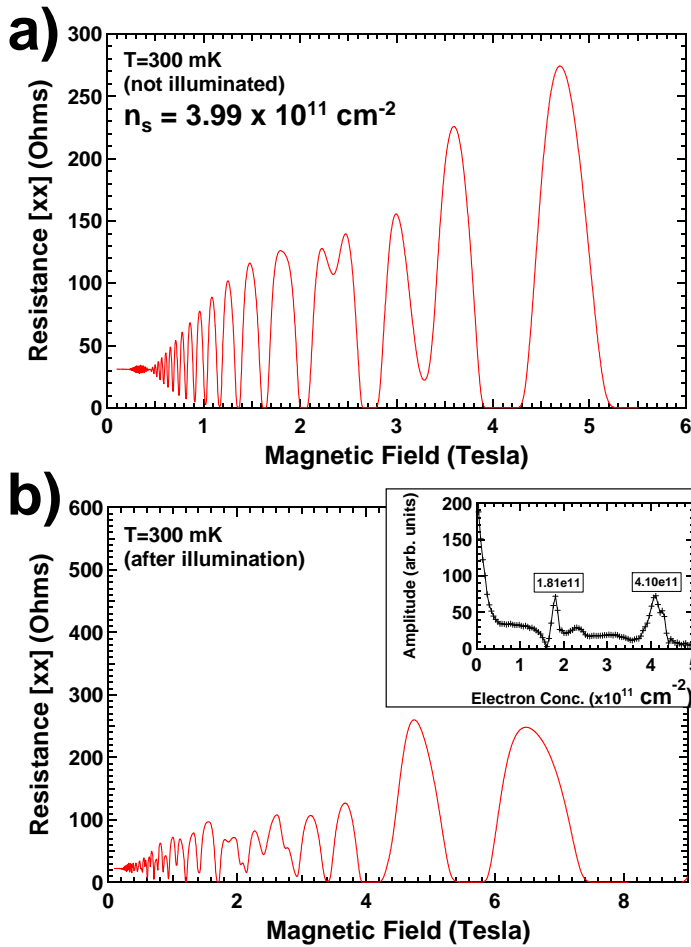


Figure 13: a) Shubnikov de-Haas oscillations from a sample doped like Q2 exhibit well-resolved spin-split Landau levels in a pattern consistent with only one well being filled with electrons prior to illumination with a red LED. b) After illumination, the pattern of oscillations changes as additional carriers become available to fill the well closer to the sample surface. A straightforward Fourier analysis of the data plotted vs. inverse field is inset and shows a second periodicity corresponding to the electron density in the upper well (peak at $1.8 \times 10^{11} \text{ cm}^{-2}$).

taking a Fourier transform of the data plotted as a function of inverse field, two periodicities are observed. The second periodicity arises from the fact that upon illumination, additional carriers are created and trapped in the upper well. Prior to illumination, only one periodicity is observed, hence, we were confident that the samples were grown to the proper specifications and the doping spanned the range of values we intended. Q1, Q2, and Q3 were then submitted to the process engineers for fabrication into SQLG devices.

Prototype SQLG devices were fabricated on long rectangular mesas etched down to the InP substrate onto which a thin (30 nm) Si_3N_x dielectric was deposited. Ohmic contacts were annealed at either end of the mesa, along with side contacts used to eliminate lead resistances from the measurements. A layer of Ti/Pt/Au was deposited onto and into a hole etched in the dielectric at the center of the mesa. Tri-level photoresist was deposited on the entire structure and electron-beam lithography was used to develop a mold into which more Ti/Pt/Au metallization was deposited to form the air-bridged gate structure. A close-up view of the gate area is shown in Fig. 14. In Fig. 14a, a model showing the configuration of the QPC gates (L and R) and the quantum dot gate electrode (air bridge structure) can be seen. Current flows right to left in the figure through the QPC

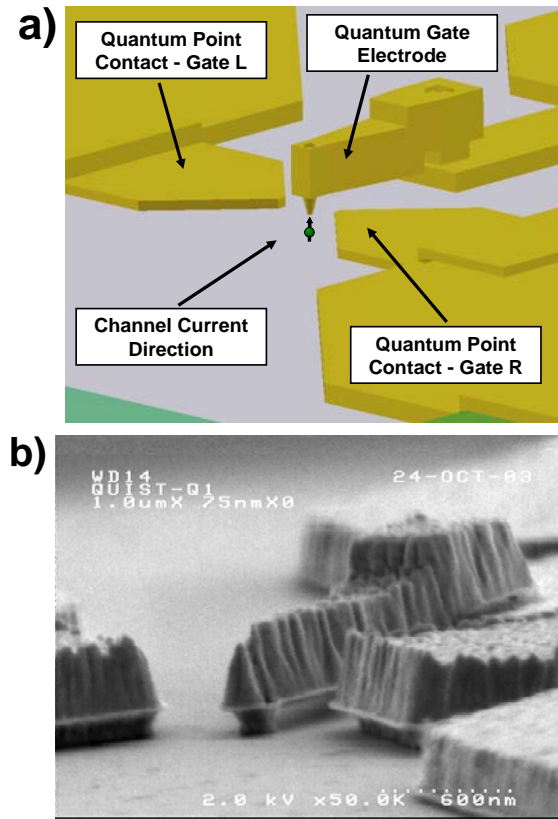


Figure 14: a) Model of the HRL single-qubit logic gate (SQLG) showing quantum point contact gates (L and R) and the gate electrode. The qubit is represented by an electron drawn into the upper quantum well by the quantum gate. The presence of the electron is detected through the influence of its charge on the conductance of the lower quantum well in the region constricted by the quantum point contact gates. b) SEM micrograph of a typical device from the wafer Q1 shows space under the air bridge and slight undercutting of the quantum point contact gates. The gate diameter is approximately 200 nm.

gates under normal operation. Negative bias is applied to the QPC gates, while positive bias on the quantum gate draws the electron qubit into the upper well. Fig. 14b shows a scanning electron micrograph (SEM) image, taken from one of the devices fabricated from Q1. The dimension of the gate is roughly 200 nm. The smallest gates we made measured about 50 nm in diameter. A slight undercutting of the QPC gates is also seen in Fig. 14b. A modification to the electron-beam lithography exposure sequence was found during the processing of Q2 to virtually eliminate this problem.

(5.2.3) Demonstration of single-electron sensitivity in top-gated InGaAs/InP quantum dot devices

As long as the electrons occupying the quantum dot remain in place long enough (on the order of several hundred milliseconds) our detection setup should be capable of detecting single-electron tunneling events. For this reason, we increased the spacer thickness in the nominal structures from the 10.6 nm used previously in Q1, Q2, and Q3 to 30 nm in the present design. The expectation was that as electrons tunneled into the dot sequentially, we would observe discontinuous jumps in the conductance of the channel due to Coulomb repulsion. This is exactly what we have now observed.

In Fig. 15, we plotted differential conductance (dI/dV_{SD}) as a function of gate voltage for a 50 nm quantum dot located at the center of a 1 μm wide QPC. The data were taken using a PAR 124A lock-in amplifier with the reference applied through a resistor divider network. In this way, 22 nA AC current was applied to the sample at 190 Hz. With -3.85 V applied to the QPC and zero bias on the gate (dot), this particular device was pinched off (zero conductance), as can be seen in the figure. By increasing the gate voltage, the channel became conducting. Above 0.8 V, a noticeable change in the signal-to-noise ratio was observed.

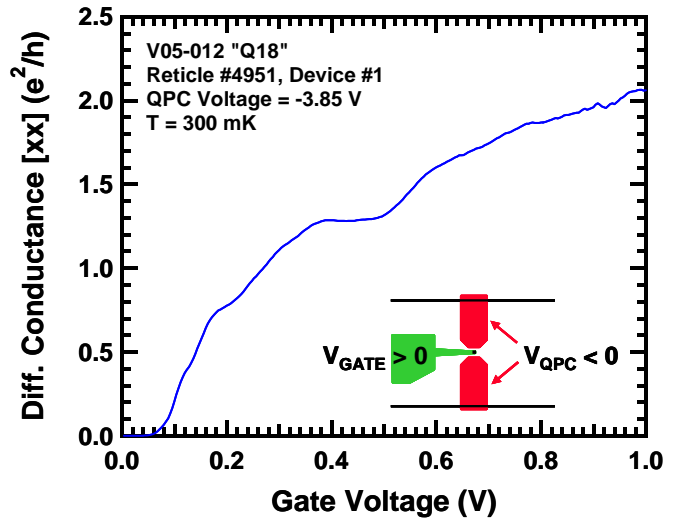


Figure 15: Differential conductance (dI/dV_{SD}) as a function of gate voltage for a 50 nm dot in a 1 μm gap between two leads of a quantum point contact (QPC). The data were obtained for a double-quantum well structure containing InGaAs wells in an InP matrix. Reproducible structure (plateaus) is notable in addition to “noise” appearing at 0.8 V and higher in gate voltage. The QPC was held at a large negative bias to deplete the channel under the dot.

By slowing down the sweep rate and taking many more points, the “noise” observed in the data for Fig. 15 began to look much more like steps. In Fig. 16, we show four sweeps over the same range in gate voltage with the QPC voltage still fixed at -3.85 V. The data reveal discontinuous jumps to lower values of differential conductance. These jumps can be identified with single-electron transitions. Since few events were observed below 0.7 V gate bias, we believe that the quantum dot was indeed in the few-electron occupancy regime.

In Fig. 16(b), we have expanded the scale to show more clearly the individual levels corresponding to the zero and higher electron states of the quantum dot. The transitions are clearly separated in gate voltage and reproducible, from trace-to-trace. Impressively, one can follow the transitions on any particular trace and count electrons tunneling into the dot one-by-one, up to as many as 15 electrons! This is quite remarkable and demonstrates a level of control that we were extremely excited to see.

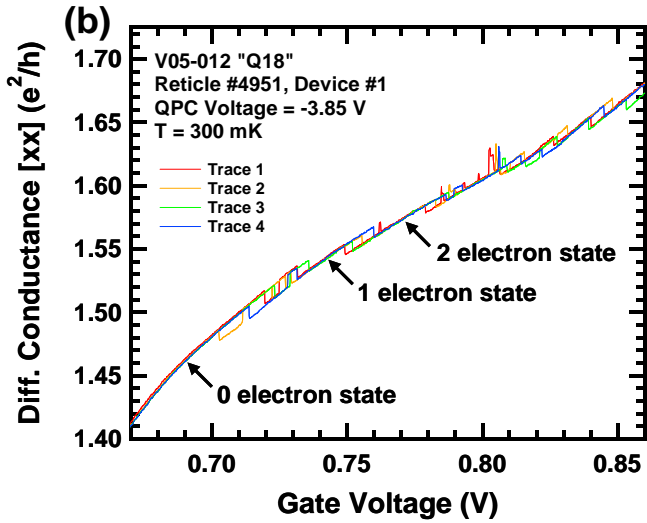
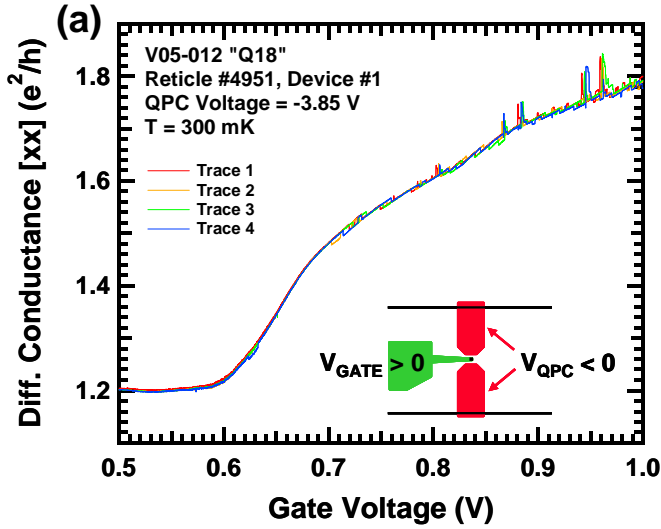


Figure 16: (a) dI/dV_{SD} obtained from the same device as described in Fig. 15 at a significantly reduced sweep rate and increased point density. The data reveal transitions between multiple levels of conductance which we tentatively associate in (b) with the zero electron, one electron, and two electron states of the quantum dot. With the arrival of each successive electron, the conductance of the quantum well below it decreases in discrete steps.

These tests have convinced us that we were dealing with extremely long tunneling times (on the order of several minutes) and there were only a few electrons on the dot.

In Fig. 17, we plotted differential conductance as a function of time for fixed gate voltage and QPC voltage. The gate was held at +1.0 V, a rather high value for which several (perhaps 7 or 8 electrons) were on the dot. In the figure, one can see the conductance switch back and forth between basically two levels in a random pattern reminiscent of a random telegraph signal (RTS) but over a long timescale. This behavior can be attributed to single electrons tunneling into and out of the dot once every few minutes or so. The two spikes appear to be events during which suddenly all of the electrons are forced to jump out of the dot and return one-by-one to the

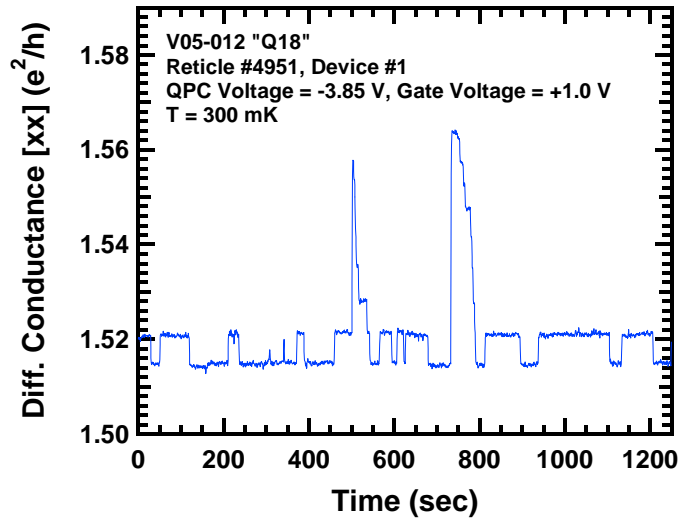


Figure 17: Differential conductance vs. time under fixed bias conditions shows random fluctuations in the dot occupancy by \pm one electron (random telegraph signal). The average time between events is on the order of several minutes, due to the rather large (30 nm) spacing between the dot and the lower quantum well in this particular device structure. Two multiple-electron events are also observed and are now believed to be caused by unintentional spikes in the gate voltage.

previous level of occupation. These events have been traced to momentary electromagnetic interference or line voltage fluctuations which caused 100 μ s long spikes in the gate voltage.

(5.2.4) First demonstration of few-electron quantum dot spectroscopy using random telegraph analysis

During the last year of the program, we focused our attention on the single event transitions we had observed previously in our SQLG devices. Recall that in these devices, electrons are induced to tunnel through an InP spacer layer from the detecting 2DEG and into the quantum dot. Therefore, decreasing the spacer thickness should increase the tunneling rates. For the devices made using the 30 nm InP spacer, the tunneling rates were too long, making a quantitative study nearly impossible. Here, we describe experiments on a device made from a structure with only a 15 nm thick spacer, resulting in much faster tunneling rates (one event every second or less).

The faster tunneling rates in these devices means that some transitions may not appear as discrete jumps but rather as small inflections in the channel current as a function of gate voltage. Discontinuous jumps are only resolvable if the measurement bandwidth is higher than the lifetimes of the particular states of the quantum dot involved in the transition. In our experiments, we used the reference signal from a Stanford Research SR830 digital lock-in amplifier to source a small AC current at 2 kHz through the channel under our quantum dot. We used a voltage divider to provide a 40 μ Vrms AC excitation to one end of the channel and connected the other end to the current input on the lock-in (virtual ground). The lock-in time constant was set to 30 ms and therefore limited the bandwidth of the measurement to a little more than 30 Hz. Signal-to-noise ratio considerations prevented us from increasing the bandwidth any further.

In Fig. 18, we show the current as a function of gate voltage for a SQLG device with a 1 μ m wide QPC and a 100 nm diameter dot electrode. The voltage on the QPC was set to -4.30 V. Clearly visible are inflections and occasional discrete jumps associated with single-electron tunneling from the channel into the quantum dot. The slowest transitions are shown in the three insets with the transition near 1.2 V corresponding to an N to N+1 transition with $N \approx 8$. This particular transition was slow enough for us to resolve individual tunneling events as we stepped the gate voltage and sampled the current as a function of time to generate a random telegraph signal (RTS). Due to the thinner spacer layer, timescales are now short enough to gather good statistics and extract quantitative information. The signal to noise ratio was sufficient to allow for extraction of lifetime data.

In Fig. 19, we plotted the current as a function of time for three gate voltages spanning the width of the transition near 1.2 V. In each case, the current was observed to jump between two levels, corresponding to a transition from the N electron state (higher current) to the N+1 electron state (lower current) and vice-versa. The data for $V_{\text{GATE}} = 1.174$ V are offset slightly for clarity. The full set of data were obtained by stepping the gate voltage in 2 mV steps between 1.160 and 1.180 V and sampling the current in 1 sec intervals for 1 hour. At $V_{\text{GATE}} = 1.170$ V, the lifetime of the N and N+1 electron states are roughly equal. For voltages less than

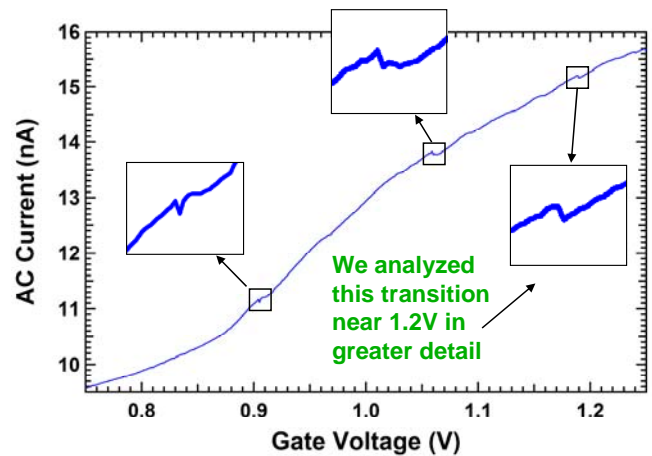


Figure 18: Current vs. gate voltage for a SQLG device fabricated using a structure with a 15 nm spacer between the detecting 2DEG and the quantum dot. The QPC voltage was set to -4.30V. The data were taken by applying the reference signal of an SR830 lock-in amplifier through a voltage divider to provide an AC excitation of 40 μ Vrms. The frequency and the lock-in time constant were set to 2 kHz and 30 ms, respectively.

1.170 V, the dot is primarily in the N electron state and for voltages greater than 1.170 V, it is mostly in the N+1 electron state. The distribution of lifetimes was determined to obey simple Poisson statistics. This is a well understood phenomenon, observed for years in MOSFET traps [5] and more recently in quantum dots [6].

An analysis of the data set allowed us to extract a variety of information about the transitions and further supports our conclusion that electrons are tunneling between the gate-induced quantum dot and the readout channel below. We began by writing an algorithm to ignore the relatively small background drift in the current and output a list of the length of time the dot is in one state vs. the other. The distribution of times were binned and plotted in terms of the probability that the state is N or N+1 for a given length of time. On a semilog plot, the data for each gate voltage are roughly linear, as expected for Poisson statistics and the fit to the data provides a measure of the lifetime of that state. The lifetimes are plotted in Fig. 20 along with their ratio.

As a function of gate voltage, we found that only the ratio of the lifetimes varies monotonically. The lifetimes actually increase anomalously, near the middle of the transition. We surmised that this phenomenon reflects kinetics as opposed to thermodynamics. In equilibrium, the ratio for each gate voltage should be predictable and reflect the relative occupancy of the states. In fact, the occupancy probability is easily derived from a grand canonical ensemble formalism $Z = \sum_{\{s,N\}} g_s e^{-\beta(E_s - NE_F)}$ where $\beta=1/kT$, E_F is the Fermi energy (chemical potential),

g_s is the degeneracy (orbital and/or spin) of the state s , and the summation is over all possible electronic states and possible numbers of electrons, N . Then, the probability of configuration i is $p(N_i, E_i) = \frac{1}{Z} g_i e^{-\beta(E_i - N_i E_F)}$.

Now consider a system with two states of charge involving energy levels N and $N+1$. Assume $E_N = 0$ (arbitrary) and take E_{N+1} to be the energy at which the system transitions to the $N+1$ state. Then the partition function for this two state system is $Z = g_N e^{\beta N E_F} + g_{N+1} e^{-\beta(E_{N+1} - (N+1)E_F)}$. Then the probability of occupying the

state $N+1$ is given (with $g = \frac{g_N}{g_{N+1}}$) by $p_{N+1} = [1 + g e^{\beta(E_{N+1} - E_F)}]^{-1}$. The ratio of lifetimes can then be interpreted

as the occupancy ratio $\frac{\tau_h}{\tau_l} = \frac{1 - p_{N+1}}{p_{N+1}} = g \exp((E_{QD} - E_F)/kT)$. This ratio is the exponential in the energy

difference between the $N+1$ quantum dot state and the Fermi energy. The fit to the experimental data assumes that the energy difference is linear in the gate voltage over this narrow range.

Increasing the gate voltage moves the energy level of the dot relative to the Fermi energy. A fit to the data in Fig. 20 tells us how the energy level of the dot state relative to the Fermi level varies with gate voltage. This can be compared with device simulation results. We measure therefore a $\Delta E_{QD}(V_{GATE}) = 9 \text{ meV} * V_{GATE}$ at 300

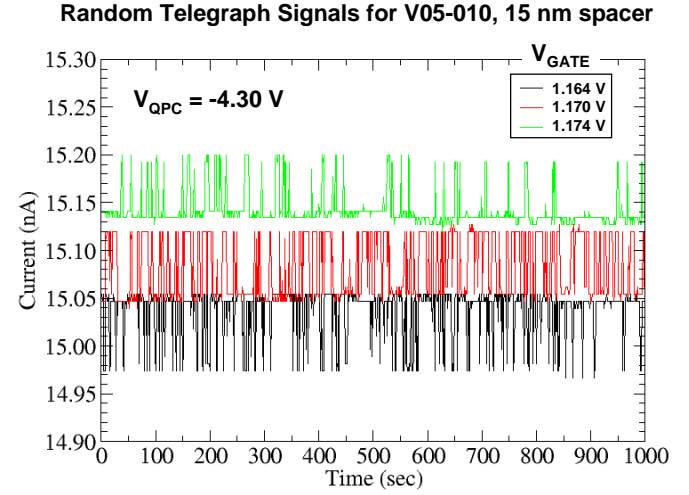


Figure 19: Current as a function of time at fixed gate voltage. At $V_{GATE} = 1.170 \text{ V}$, the lifetimes for the N electron state and the N+1 electron state of the quantum dot are roughly equal. For $V_{GATE} = 1.164 \text{ V}$ (1.174 V), the number of electrons on the dot is primarily N (N+1). The distribution of lifetimes obeys simple Poisson statistics.

mK. This compares to the theoretical prediction of $12 \text{ meV} * V_{\text{GATE}}$. This is completely equivalent to measuring the width of a Coulomb blockade peak.

We also have calculated tunneling rates associated with the single electron charging events in these devices. Tunneling rates were computed using Fermi's Golden Rule based on numerical eigenstates derived from fully 3-dimensional self-consistent Poisson-Schrodinger calculations. The effects of Coulomb interaction on the quantum dot states and hence tunneling rates was considered. A comparison of these numerical results with experimental estimates of tunneling rates derived from random telegraph signals indicates that the observed tunneling rates are considerably slower than expected from theory. Determining the cause of this discrepancy will be part of a future research program.

In summary, RTS has been observed in enhancement mode quantum dots formed by a single gate placed in forward bias. All data are consistent with single electron charging of a quantum dot. This demonstrates basic proof of principle of this device. The RTS rate for some of the transitions is in the range that allows for good statistics to be obtained. The tunneling rates are slow enough to be resolved by our several tens of Hz bandwidth measurement system, and fast enough to allow for accumulation of good statistics in a reasonable amount of time (hours). Analysis of the data shows that the lifetimes are Poisson distributed, as expected. The ratio of occupancies was found to be exponential in gate voltage and the width of the transition (inferred from the slope) agrees with theoretical estimates assuming a 300 mK electron temperature.

(5.3) Control accomplishments

The initial control effort was centered on developing a simulation model of the essential features of the proposed spin-coherent photon transmitter/receiver system. The purpose of the model is to evaluate control strategies for creating the requisite quantum logic gates. In particular, the control design goal is to make an EPR pair – the Bell states. Input preparation and photon/electron interactions were not initially included. Emphasis was placed on modeling sources of uncertainties in the system, e.g., uncertain parameters, fringe effects, and sources of decoherence such as nuclear spin.

The control variables in the model are the external potentials (gate voltages) which directly effect the g-factors in the semiconductor material in the presence of an external magnetic field. The g-factors are used to control the electron spin states. Preliminary results indicated that some implementations of the logic gates needed to execute the teleportation algorithm place constraints on the design of the device.

Various control strategies were evaluated in simulation in order to map out a robust design space. The design approaches included pulse methods similar to those used in NMR as well as optimal control design. The latter approach is much easier to implement in this device than in NMR, for example, because the driving fields are applied to gate voltages rather than magnetic fields.

Lifetimes of High and Low Current States

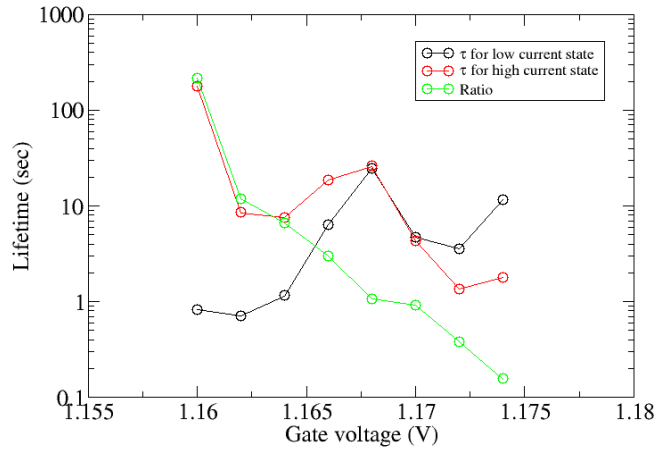


Figure 20: Lifetime of the N electron state (high current) vs. the N+1 electron state (low current) as a function of gate voltage for the transition studied in Fig. 19. A monotonic decrease in the ratio of the lifetimes is observed, with a slope consistent with device simulation results.

In the second year of the program, we examined the electron/nuclei interaction as a source of decoherence. Proposed models found in the literature produce decoherence through an interaction that behaves like a measurement, i.e., the electron/nuclei interaction is dependent on the magnitude of the electron wave function. Assuming this interaction is relatively small, we studied the use of linearized models to obtain optimal corrections to control pulses designed without the interaction.

We also concentrated on developing and refining methods for quantum tomography and quantum state detection. A number of problems in quantum state estimation (state tomography), quantum system identification (process tomography) and quantum state and system detection can be cast as convex optimization problems. The great advantage of convex optimization is a globally optimal solution can be found efficiently and reliably, and perhaps most importantly, can be computed to within any desired accuracy using an interior-point method.

Some of these problems are already known to be convex but have not fully exploited the available convex solvers or duality theory. For example, it is known that Maximum likelihood Estimation (MLE) of the quantum state (density) is a convex optimization. What we also showed is that a number of other MLE problems are convex, e.g., estimating the distribution of known states and quantum process tomography in the Kraus operator sum representation (OSR) in a fixed basis. One important problem that is not convex is MLE of Hamiltonian parameters. We showed, however, how duality theory can help establish bounds on the parameter estimates for this problem.

Another problem that can be solved via convex optimization is experiment design. (Experiment design here means choosing the number of experiments to be performed in a particular system configuration; a configuration being any number of combinations of sample times, hardware settings, etc. For example, in quantum state photonic tomography, we can determine the optimum number of wave plate settings to achieve a desired estimation accuracy.) We have been able to apply the experiment design procedure invoked by the Cramer-Rao Inequality to all the MLE problems mentioned above, including MLE of Hamiltonian parameters. In all these cases, the optimum experiment design problem, although integer-combinatoric, can be relaxed to a convex optimization problem whose solution provides upper and lower bounds on the unknown optimal integer solution. The MLE of the state or process can be combined with the optimal experiment design in a "bootstrapping" iteration to make the estimation more efficient.

We have addressed the problem of designing a detector that is maximally sensitive to specific quantum states. The design problem can be formulated as a convex optimization problem in the matrices of the POVM (positive operator valued measure) that characterize the measurement apparatus, or with a given POVM, the matrices which characterize the OSR in a fixed basis. We specifically addressed maximizing the posterior probability of detection and showed that this is a quasiconvex optimization problem in either the POVM or OSR matrices. Previous work in this area has only considered the joint probability of detection over POVM matrices,

In all the cases described above we showed how duality theory can be used in various special cases to give insight into the nature (and possible physical implementation) of the optimal solutions.

To make quantum information systems robust will require that the systems operate under some form or combination of control and error correction. Moreover, it is highly likely that in order to achieve the desired system objectives, these systems will have to be tuned, or even entirely determined, using estimated quantities obtained from data from the actual system rather than solely relying on an initial design from a theoretical model. To alleviate these concerns, we have been developing the mathematical and computational tools for quantum state and process tomography as well as quantum state detection.

For quantum state detection the goal is to design the measurement apparatus to determine whether or not a particular state was present in the input to the detector. The problem is thus equivalent to the design of a quantum channel that optimally transforms the input state distribution (assumed to be given, and including non-orthogonal states) to the output measurement outcomes. The channel may be lossy, and may introduce noise, and thus there may be latency in the measurement, in which certain outcomes are ambiguous. Previous work in this problem has shown that maximizing the average conditional probability over the set of all possible measurement devices is a convex optimization, specifically what is called an SDP, or Semidefinite Program. We have found that maximizing the posteriori probability over all possible measurement apparatuses is also convex, specifically quasiconvex and therefore also solved via convex programming. The posteriori probability, which answers the question: if detector declares that state is present, what is the probability that it is actually present. We developed software for solving this problem.

We also investigated the problem of generating the control signals to activate the quantum logic gates. At present we see this as a classical control and signal processing problem. The main difficulty is that the interconnects become very dense as they approach the geographical quantum gate location and this density gives rise to “cross-talk” across the different channels. More precisely, at the gigahertz frequencies required for quantum gate operation, the interconnect system behaves exactly like a multi-input multi-output transmission line. The problem is further compounded by uncertainties arising from manufacturing variations in the quantum gate impedances as well as in the interconnects.

We are specifically interested in determining the limit of performance possible for such a system. We explored several approaches:

(1) Open-loop robust control

Design the controls using prior knowledge or estimates of the interconnect/quantum gate system and uncertainty ranges.

(2) Open-loop adaptive control

Design the controls using knowledge or estimates of the interconnect/quantum gate system obtained from on-line measurements and experiments specifically created for obtaining such knowledge.

(3) Closed-loop control

Use real-time feedback from the interconnect/quantum gate system to regulate the control signals to the gates.

To make the problem more concrete we starting with the assumption that the interconnect system, not including the quantum gate impedances, can be very well modeled or estimated from on-line data. The main source of uncertainty is thus the impedance to the quantum logic gates. Even knowing the interconnect system, however, does not mean signals can be created to perfectly invert the dynamics. There is a limit to bandwidth and signal timing that is possible and certainly made more difficult when the quantum gate impedances are uncertain. One saving grace is that the gate uncertainties are likely to be systematic rather than continuously random variations. Thus once identified, the problem becomes one of inversion.

Towards this end we concentrated on approach using closed-loop control. The first issue is how to generate a feedback signal. Adding more interconnects to obtain measurements obviously compounds the problem in several ways. First it increases the possibility of more uncertainty and more cross-talk. Secondly, it requires more geography, which may reduce cross-talk. A simpler approach is to take advantage of the transmission line

bi-directional capabilities. In this regard we have conceived of a method to use the reflected waves as feedback. This has the disadvantage of adding signal delay. However, the system uncertainty has not been increased thereby making robust inversion more possible, modulo the additional delay. We need also account for uncertainties from this measurement scheme arising from noise and/or uncertain measurement dynamics. The goal of this investigation was to not only understand the performance limits but also to develop design tools which can be utilized for any proposed system.

Finally, we have applied methods of convex optimization to the design of quantum error correction (QEC). Convex optimization has proven very powerful in our previous efforts in state and process tomography [quant-ph/0411093] and quantum state detection [quant-ph/0403150]. For QEC it remains an open question as to whether errors can be dealt with more efficiently in tailored system configurations that do not require the full level of complexity attendant to standard QEC.

We have shown that the problem of designing a quantum information error correcting procedure can be cast as a bi-convex optimization problem, iterating between encoding and recovery, each being a semidefinite program (SDP) [quant-ph/0606078]. For a given encoding operator, the problem is convex in the recovery operator. For a given method of recovery, the problem is convex in the encoding scheme. This allows us to derive new codes that are locally optimal. We now have examples of such codes that can handle errors that are too strong for codes derived by analogy to classical error correction techniques. We have also shown that the dual optimization, also an SDP, is of lower complexity and thus requires less computational effort. The SDP formalism also allows for a robust design by enumerating constraints associated with different error models.

A distance measure was also developed [quant-ph/0606064] between two unitary propagators of quantum systems of differing dimensions along with a corresponding method of computation. A typical application is to compare the propagator of the actual (real) process with the propagator of the desired (ideal) process; the former being of a higher dimension than the latter. This measure has the advantage of dealing with possibly correlated inputs, but at the expense of working on the whole space and not just the information bearing part as is usually the case, i.e., no partial trace operation is explicitly involved. This distance measure and an average measure of channel fidelity both depend on the size of the same matrix: as the matrix size increases, distance decreases and fidelity increases.

(6) Bibliography

- [1] R. Vrijen and E. Yablonovitch, "A Solid-State Spin-Coherent Photo-Detector for Quantum Communication," *Physica E* **10**, 569 (2001).
- [2] A. A. Kiselev, E. L. Ivchenko, and U. Rössler, "Electron g Factor in One- and Zero-Dimensional Semiconductor Nanostructures," *Phys. Rev. B* **58**, 16353 (1998).
- [3] A. Trellakis, A.T. Galick, A. Pacelli and U. Ravaioli, "Iteration Scheme for the Solution of the Two-Dimensional Schrödinger-Poisson Equations in Quantum Structures," *J. Appl. Phys.* **81**, 7880 (1997).
- [4] M. Dobers, "Electron Spin Resonance and Overhauser Shift of Two-Dimensional Conduction Electrons," *Surf. Sci.* **229**, 126 (1990).
- [5] M. J. Kirton and M. J. Uren, "Noise in Solid-State Microstructures: A New Perspective on Individual Defects, Interface States and Low-Frequency ($1/f$) Noise," *Adv. Phys.* **38**, 367 (1989).
- [6] S. Gustavsson, R. Leturcq, B. Simović, R. Schleser, T. Ihn, P. Studerus, and K. Ensslin, "Counting Statistics of Single Electron Transport in a Quantum Dot," *Phys. Rev. Lett.* **96**, 076605-1 (2006).

MASTER COPY: PLEASE KEEP THIS "MEMORANDUM OF TRANSMITTAL" BLANK FOR REPRODUCTION PURPOSES. WHEN REPORTS ARE GENERATED UNDER THE ARO SPONSORSHIP, FORWARD A COMPLETED COPY OF THIS FORM WITH EACH REPORT SHIPMENT TO THE ARO. THIS WILL ASSURE PROPER IDENTIFICATION. NOT TO BE USED FOR INTERIM PROGRESS REPORTS; SEE PAGE 2 FOR INTERIM PROGRESS REPORT INSTRUCTIONS.

MEMORANDUM OF TRANSMITTAL

U.S. Army Research Office
ATTN: AMSRL-RO-BI (TR)
P.O. Box 12211
Research Triangle Park, NC 27709-2211

- | | |
|--|--|
| <input type="checkbox"/> Reprint (Orig + 2 copies) | <input type="checkbox"/> Technical Report (Orig + 2 copies) |
| <input type="checkbox"/> Manuscript (1 copy) | <input type="checkbox"/> Final Progress Report (Orig + 2 copies) |
| | <input type="checkbox"/> Related Materials, Abstracts, Theses (1 copy) |

CONTRACT/GRANT NUMBER:

REPORT TITLE:

is forwarded for your information.

SUBMITTED FOR PUBLICATION TO (applicable only if report is manuscript):

Sincerely,